

## Kinematic simulations of dynamo action with a hybrid boundary-element/finite-volume method

*A. Giesecke, F. Stefani, G. Gerbeth*

*Forschungszentrum Dresden – Rossendorf, Department Magnetohydrodynamics, POB 51 01 19, D – 01314 Dresden, Germany*

The experimental realization of dynamo excitation as well as theoretical and numerical examinations of the induction equation have shown the relevance of boundary conditions for a self-sustaining dynamo. Within the interior of a field producing domain geometric constraints or varying material properties (e.g. electrical conductivity of the container walls or localized high-permeability material) might also play a role. Combining a grid based finite volume approach with the boundary element method in a hybrid FV-BEM scheme offers the flexibility of a local discretization with a stringent treatment of insulating magnetic boundary conditions in almost arbitrary geometries at comparatively low costs. Kinematic simulations of dynamo action generated by a well known prescribed mean flow demonstrate the reliability of the approach.

Future examinations are intended to understand the behavior of the VKS-dynamo experiment where the field producing flow is driven by ferrous propellers and the induction effects of conductivity/permeability inhomogeneities might provide the required conditions for the measured dynamo characteristics.

**Introduction.** Nowadays, there are nearly no doubts that the mechanism which is responsible for the generation of astrophysical or planetary magnetic fields is a dynamo process in which kinetic energy from a suitable flow of a conducting fluid is transferred into magnetic energy. Although the basic idea of this process has already been presented at the beginning of the 20th century [1] only few years ago fluid flow generated dynamo action has been realized in the laboratory [2, 3, 4]. The key parameter that determines the onset of dynamo action is the magnetic Reynolds number  $Rm = \mu_0 \sigma VL$  where  $\sigma$  denotes the electrical conductivity,  $\mu_0$  the vacuum permeability,  $V$  a typical velocity magnitude and  $L$  the characteristic size of the considered system. Critical values that are necessary to obtain dynamo action in the laboratory are of the order  $Rm^{\text{crit}} \sim 30 \dots 100$  which is already technically demanding. Therefore, essential efforts are concentrated on possibilities to reduce this critical value and to increase the actual  $Rm$  of the field producing flow.

From numerical simulations it is known that the boundary conditions and also boundary layers of stagnant or somehow guided flow could possess supportive as well as obstructive impacts on the onset of dynamo action [5, 6]. In the kinematic regime the backreaction of the field on the flow by the Lorentz force can be ignored so that the complexity of the underlying system of equations is significantly reduced because only the induction equation with a prescribed velocity field has to be solved numerically. Nevertheless, analyzing laboratory experiments requires a flexible numerical scheme that is able to consider geometric constraints as well as material properties like conductivity jumps between fluid and container walls or the high-permeability domains brought in by the iron propellers that are used to drive the flow in the VKS experiment, at least in the realization which showed dynamo action up to present [4]. The finite volume (FV) approach provides a fast and robust scheme relying on a local discretization which delivers an accurate solution of the kinematic dynamo problem and intrinsically maintains the solenoidal

character of the magnetic field [7]. However, a drawback of grid based schemes are the difficulties arising from non-local boundary conditions as they exist in the laboratory in terms of insulating boundaries. Insulating boundary conditions in non-spherical geometry, in general, are treated by elaborated schemes, e.g. solving of the Laplace equation in an extended domain and applying some matching conditions [8, 9, 10], embedding the domain in a sphere [11] or by simplifying approximations (pseudo vacuum, vanishing tangential field). Rather precise results which consider insulating boundary conditions exactly are provided by the integral equation approach [12, 13]. However, the application possibilities are limited because of enormous computational resources that are required by this method. A different approach that needs less computational power is known as the boundary element method (BEM) [14]. Outside the conducting region, the magnetic flux density  $\mathbf{B}$  is expressed as the gradient of a scalar potential  $\mathbf{B} = -\nabla\Phi$ , where  $\Phi$  is determined by the Laplace equation:  $\Delta\Phi = 0$ . Making use of Greens second theorem and an appropriate discretization, the Laplace equation is integrated only on the boundary which in the numerical implementation requires the solution of an algebraic set of equations. A combined finite volume/boundary element method (FV-BEM) for the induction equation was introduced in [15]. The presented applications were restricted, however, to the decay of an initial homogenous magnetic field. A deeper investigation of the reliability of the numerical approach in case of more complex and realistic problems like dynamo action is still missing.

The scope of the present paper is the introduction of the methods and basic properties of the combined finite volume/boundary element method. The resulting scheme is adopted for the numerical solution of the kinematic induction equation in cylindrical coordinates in three dimensions with emphasis on the implementation of insulating boundary conditions. The integration of further physical effects like small scale induction effects parameterized by an  $\alpha$ -effect (small scale helical turbulence) are easily carried out and an extension to a scheme that considers variations and/or jumps in conductivity ( $\sigma$ ) respectively permeability ( $\mu_r$ ) is straightforward if corresponding averaging procedures for  $\sigma$  or  $\mu_r$  are applied so that the jump conditions for  $\mathbf{E}$  and  $\mathbf{B}$  at material interfaces are fulfilled [16]. The detailed description of the corresponding methods is beyond the scope of this publication and will be presented in a subsequent paper.

## 1. Equations and numerical methods.

*1.1. Finite volume method.* From Faraday's law  $\partial_t\mathbf{B} = -\nabla \times \mathbf{E}$  with the magnetic flux density  $\mathbf{B}$  and the electric field  $\mathbf{E}$  given by

$$\mathbf{E} = -\mathbf{v} \times \mathbf{B} + \frac{1}{\sigma\mu_0} \nabla \times \frac{\mathbf{B}}{\mu_r} \quad (1)$$

one immediately retrieves the induction equation

$$\frac{\partial\mathbf{B}}{\partial t} = \nabla \times \left( \mathbf{v} \times \mathbf{B} - \frac{1}{\sigma\mu_0} \nabla \times \frac{\mathbf{B}}{\mu_r} \right). \quad (2)$$

Here,  $\mathbf{v}$  denotes the velocity field,  $\sigma$  the electric conductivity,  $\mu_0$  the vacuum permeability given by  $\mu_0 = 4\pi \times 10^{-7} \text{VsA}^{-1}\text{m}^{-1}$  and  $\mu_r$  the relative permeability, that describes the ability of the magnetic flux to penetrate a medium. For most substances like air or non-ferrous conducting materials (copper, sodium)  $\mu_r$  is very close to 1 whereas ferrous material exhibits a relative permeability in the range of  $\mu_r \sim 10^2 \dots 10^4$ . In the following, only homogenous ( $\sigma = \text{const}$ ),

non-ferromagnetic ( $\mu_r = 1$ ) materials are considered. In a finite volume method the computational domain is divided into (small) control volumes where the conservation of all variables is enforced across the control surfaces (interfaces between neighboring cells). Writing the induction equation in conservative form  $\partial_t \mathbf{B} + \nabla \times \mathbf{E} = 0$ , the update of the  $x$ -component of magnetic field at a timestep  $n + 1$  in a Cartesian system is given by

$$B_{ix-\frac{1}{2},iy,iz}^{x,n+1} = B_{ix-\frac{1}{2},iy,iz}^{x,n} + \frac{\delta t}{\Delta y} \left( E_{ix-\frac{1}{2},iy+\frac{1}{2},iz}^{z,*} - E_{ix-\frac{1}{2},iy-\frac{1}{2},iz}^{z,*} \right) - \frac{\delta t}{\Delta z} \left( E_{ix-\frac{1}{2},iy,iz+\frac{1}{2}}^{y,*} - E_{ix-\frac{1}{2},iy,iz-\frac{1}{2}}^{y,*} \right). \quad (3)$$

In Eq. (3)  $\mathbf{E}^*$  denotes the electric field at an intermediate time step: in an explicit scheme with second order accuracy  $*$  represents the time after the update of the predictor step whereas in an implicit scheme  $*$  represents the actual timestep  $n + 1$ . As indicated by the indices, the localization of the components of  $\mathbf{E}$  is slightly staggered with regard to the components of  $\mathbf{B}$ . Fig. 1 shows the position of the field components around a single grid cell labeled  $(ix, iy, iz)$ .

Vector quantities are defined on the faces ( $\mathbf{B}$ , labeled by one half-integer index) respectively on the edges of a grid cell ( $\mathbf{E}$ , labeled by two half-integer indices) whereas scalar quantities like conductivity/permeability are defined at the center of a grid cell. It is convenient to decompose the electric field into an inductive part  $\mathbf{E}^{\text{ind}} \propto \mathbf{v} \times \mathbf{B}$  and a diffusive part  $\mathbf{E}^{\text{diff}} \propto (\mu_0 \sigma)^{-1} \nabla \times \mathbf{B}$ .  $\mathbf{E}_{\text{ind}}$  is treated explicitly applying the C-MUSCL method introduced in [7]. Here, only the basics of the scheme are rewritten exemplary for single components of the involved quantities. In a predictor step (at an intermediate timestep  $n + 1/2$ ) the magnetic field on the edges of a grid cell is computed by

$$B_{x,ix-\frac{1}{2},iy+\frac{1}{2},iz}^{n+1/2,R} = B_{x,ix-\frac{1}{2},iy,iz}^n + \left( \frac{\partial B_x}{\partial t} \right)_{ix-\frac{1}{2},iy,iz}^n \frac{\Delta t}{2} + \left( \frac{\partial B_x}{\partial y} \right)_{ix-\frac{1}{2},iy,iz}^n \frac{\Delta y}{2}, \quad (4)$$

$$B_{x,ix-\frac{1}{2},iy-\frac{1}{2},iz}^{n+1/2,L} = B_{x,ix-\frac{1}{2},iy,iz}^n + \left( \frac{\partial B_x}{\partial t} \right)_{ix-\frac{1}{2},iy,iz}^n \frac{\Delta t}{2} - \left( \frac{\partial B_x}{\partial y} \right)_{ix-\frac{1}{2},iy,iz}^n \frac{\Delta y}{2}, \quad (5)$$

where the time derivative on the right hand side is computed from the known electric field  $\mathbf{E}^n$  at timestep  $n$ . The second term on the right hand side  $\partial B_x / \partial y$  is approximated using a monotonized central slope limiter which ensures positivity preserving, non-oscillating solutions:

$$\frac{\partial B_x}{\partial y} = \text{minmod} \left( \frac{B_{iy+1}^x - B_{iy-1}^x}{2\Delta y}, \text{minmod} \left( 2 \frac{B_{iy+1}^x - B_{iy}^x}{\Delta y}, 2 \frac{B_{iy}^x - B_{iy-1}^x}{\Delta y} \right) \right). \quad (6)$$

In Eq. (6)  $\text{minmod}(a, b)$  stands for the minmod limiter defined by

$$\text{minmod}(a, b) := \begin{cases} a & \text{if } |a| < |b| \text{ and } ab > 0 \\ b & \text{if } |b| < |a| \text{ and } ab > 0 \\ 0 & \text{if } ab \leq 0 \end{cases} \quad (7)$$

The electric field at the intermediate time step  $n + 1/2$  is then obtained from the

upwind solution of a 2D Riemann problem and is given by:

$$\begin{aligned}
E_{x,ix,iy-\frac{1}{2},iz-\frac{1}{2}}^{\text{ind},n+\frac{1}{2}} &= v_y \frac{B_{z,ix,iy-\frac{1}{2},iz-\frac{1}{2}}^{n+\frac{1}{2},R} + B_{z,ix,iy-\frac{1}{2},iz-\frac{1}{2}}^{n+\frac{1}{2},L}}{2} \\
&\quad - v_z \frac{B_{y,ix,iy-\frac{1}{2},iz-\frac{1}{2}}^{n+\frac{1}{2},R} + B_{y,ix,iy-\frac{1}{2},iz-\frac{1}{2}}^{n+\frac{1}{2},L}}{2} \\
&\quad - |v_y| \frac{B_{z,ix,iy-\frac{1}{2},iz-\frac{1}{2}}^{n+\frac{1}{2},R} - B_{z,ix,iy-\frac{1}{2},iz-\frac{1}{2}}^{n+\frac{1}{2},L}}{2} \\
&\quad + |v_z| \frac{B_{y,ix,iy-\frac{1}{2},iz-\frac{1}{2}}^{n+\frac{1}{2},R} - B_{y,ix,iy-\frac{1}{2},iz-\frac{1}{2}}^{n+\frac{1}{2},L}}{2} \tag{8}
\end{aligned}$$

where the magnetic field components are the time centered predicted states interpolated at the edges as determined from Eqs. (4) & (5). The final update for the magnetic field is then performed as described by Eq. (3). In comparison with a simple scheme where  $\mathbf{v}$  and  $\mathbf{B}$  on the edges of a grid cell are computed applying simple arithmetic averages, the C-MUSCL scheme allows for significant higher magnetic Reynolds numbers without becoming unstable or exhibiting oscillating solutions.

In an explicit scheme the timestep  $\delta t$  is determined by the Courant-Friedrich-Lax criteria

$$\delta t = C \cdot \min_{\text{all cells}} \left( \frac{\Delta s_{x,y,z}}{|\mathbf{v}|}, (\Delta s_{x,y,z})^2 \mu_0 \sigma \right) \tag{9}$$

with the minimum of the cell extension in  $x, y$  or  $z$  direction  $\Delta s_{x,y,z}$  and the Courant factor  $C \leq 0.5$ . From expression (9) it is immediately evident that the timestep is dominated by the diffusive part  $\propto (\Delta s)^2$  which in a cylindrical system becomes extremely small for grid cells close to the axis. To relax the constraints of the time step an implicit solver has been implemented. In a first step an intermediate magnetic field  $\mathbf{B}^*$  is computed:

$$\mathbf{B}^* = \mathbf{B}^{\text{exp}} - \delta t \nabla \times \frac{1}{\mu_0 \sigma} \nabla \times \mathbf{B}^* \tag{10}$$

where  $\mathbf{B}^{\text{exp}}$  denotes the magnetic field after the explicit update of the inductive part as described above and the diffusive part of the electric field is given in discretized form by:

$$\frac{1}{\sigma \mu_0} (\nabla \times \mathbf{B}^*)_x = \frac{1}{\mu_0 \sigma} \left( \frac{B_{ix,iy-\frac{1}{2},iz}^{y,*} - B_{ix,iy-\frac{1}{2},iz-1}^{y,*}}{\Delta z} - \frac{B_{ix,iy,iz-\frac{1}{2}}^{z,*} - B_{ix,iy-1,iz-\frac{1}{2}}^{z,*}}{\Delta y} \right). \tag{11}$$

Similar expressions can be written down for the  $y$ - and  $z$ -component.

The resulting algebraic system of equations is solved iteratively for  $\mathbf{B}^*$  using a simple Gauss-Seidel method. To remain in the framework of the finite volume scheme the electric field at time  $n + 1$  is then computed by

$$\mathbf{E}^{\text{diff},n+1} = \frac{1}{\sigma \mu_0} \nabla \times \mathbf{B}^* \tag{12}$$

which is used for the final update of the magnetic field according to Eq. (3).

1.2. *Treatment of the cylinder axis.* Although Eq. (3) describes the field update in a Cartesian system, an adoption of the scheme in cylindrical or spherical coordinates is straightforward (see e.g. [17, 18]), essentially by the application of the appropriate discretization of the operator  $\nabla \times = (1/r \partial_\varphi - \partial_z, \partial_z - \partial_r, 1/r \partial_r(r) - 1/r \partial_\varphi)$ . However, at  $r = 0$  a coordinate singularity exists that prevents the direct computation of  $B_{ir=0}^r$ ,  $B_{ir=1/2}^\varphi$  and  $B_{ir=1/2}^z$  so that these quantities have to be treated in a different way. From the requirement of regularity and uniqueness of the solution at  $r = 0$  conditions for the behavior of the magnetic field at the axis can be derived. Introducing a decomposition in azimuthal modes

$$\mathbf{B} = \Re(\mathbf{b}_m(r, z, t)e^{im\varphi}), \quad m = 0, 1, 2, 3, \dots \quad (13)$$

the behavior of the coefficients  $b_m^{r,\varphi,z}$  at  $r = 0$  is determined by the following – mode dependent – relations:

$$\begin{aligned} m = 0 : \quad b_0^r &= b_0^\varphi = \frac{\partial b_0^z}{\partial r} = 0, \\ m = 1 : \quad b_1^z &= \frac{\partial b_1^\varphi}{\partial r} = \frac{\partial b_1^r}{\partial r} = 0, \\ m \geq 2 : \quad b_m^r &= b_m^\varphi = b_m^z = 0. \end{aligned} \quad (14)$$

From these conditions the values of  $b_m^{r,\varphi,z}$  at  $r = 0$  are computed for every mode  $m$  from the values of the corresponding coefficients close to the axis. The extrapolation to the axis is based on the radial dependence of  $b_m^{r,\varphi,z}$  that follows the most general expression for vector quantities close to a cylinder axis given by (see [19])

$$\begin{aligned} B_z(r, \varphi) &= \sum_{m=0}^{\infty} r^m \left( \sum_{n=0}^{\infty} C_{mn}^S r^{2n} \right) \cos(m\varphi) + \sum_{m=0}^{\infty} r^m \left( \sum_{n=0}^{\infty} C_{mn}^A r^{2n} \right) \sin(m\varphi) \quad (15) \\ B_{r,\varphi}(r, \varphi) &= \frac{1}{r} \sum_{n=1}^{\infty} C_{0n}^S r^{2n} + \sum_{m=1}^{\infty} r^{m-1} \left( \sum_{n=0}^{\infty} C_{mn}^S r^{2n} \right) \cos(m\varphi) \\ &\quad + \sum_{m=1}^{\infty} r^{m-1} \left( \sum_{n=0}^{\infty} C_{mn}^A r^{2n} \right) \sin(m\varphi). \quad (16) \end{aligned}$$

where in the numerical realization the polynomial expansion in  $r$  is truncated at  $n = 2$ .

**2. Boundary element method.** In case of insulator conditions on the boundary the magnetic field is computed by the modified integral equation approach presented in [15]. The method depends on the ability to compute the normal component of the magnetic field on the boundary by the finite volume scheme and a conceptual proximity of the finite volume method and the boundary element method (concerning the location of the components of the magnetic field on a face centered node). The unknown tangential components of the magnetic field at timestep  $(n + 1)$  are the result of a matrix operation on a vector composed of the normal components of  $\mathbf{B}$  at the surface of the computational domain. In the following a sketch of the scheme is given.

Insulating domains are characterized by a vanishing current  $\mathbf{j} \propto \nabla \times \mathbf{B} = 0$  so that  $\mathbf{B}$  can be expressed as the gradient of a scalar field  $\Phi$  which fulfills the Laplace equation:

$$\mathbf{B} = -\nabla\Phi \quad \text{with} \quad \Delta\Phi = 0, \quad \Phi \rightarrow O(r^{-2}) \text{ for } r \rightarrow \infty. \quad (17)$$

In a volume  $\Omega$  that is bounded by the surface  $\Gamma$  Greens second identity for a scalar function  $\Phi$  and a test- or weighting function  $G$  is written as:

$$\int_{\Omega} G\Delta\Phi - \Phi\Delta G d\Omega = \int_{\Gamma} G\frac{\partial\Phi}{\partial n} - \Phi\frac{\partial G}{\partial n} d\Gamma. \quad (18)$$

If  $\Phi = 0$  the potential is determined by the integral expression

$$\Phi(\mathbf{r}) = \int_{\Gamma} G(\mathbf{r}, \mathbf{r}') \frac{\partial\Phi(\mathbf{r}')}{\partial n} - \Phi(\mathbf{r}') \frac{\partial G(\mathbf{r}, \mathbf{r}')}{\partial n} d\Gamma(\mathbf{r}'). \quad (19)$$

where  $G(\mathbf{r}, \mathbf{r}')$  is called Greens function or fundamental solution which fulfills

$$\Delta G(\mathbf{r}, \mathbf{r}') = -\delta(\mathbf{r} - \mathbf{r}') \quad (20)$$

and is given by

$$G(\mathbf{r}, \mathbf{r}') = -\frac{1}{4\pi|\mathbf{r} - \mathbf{r}'|}. \quad (21)$$

Furthermore,  $n$  represents the direction of the normal unit vector on the surface element  $d\Gamma$  and  $\partial/\partial n$  is the derivative in the normal direction:  $\partial/\partial n = \mathbf{n} \cdot \nabla$  so that  $\partial_n \Phi = -B^n$  yields the normal component of  $\mathbf{B}$  on  $d\Gamma$ . However, for  $\mathbf{r} \in \Gamma$  Eq. (19) is not valid since on the boundary  $\Phi$  does not fulfill the Hölder criteria ( $|\Phi(\mathbf{r}) - \Phi(\mathbf{r}_0)| \leq Ar^\alpha \forall \mathbf{r}$  with  $r \leq c$  and  $\alpha, c, A > 0$ ) at every point  $\mathbf{r}$ , which is an essential requirement for (18). The validity of Eq. (19) can be extended to points  $\mathbf{r} \in \Gamma$  if the integration domain around a certain source point  $\mathbf{r}$  located on the boundary is enlarged by a small half sphere with the radius  $\epsilon$  and establishing the limit  $\epsilon \rightarrow 0$  (see Fig. 2).

Writing the enlarged domain  $\Gamma' = \Gamma + \Gamma_\epsilon$  where  $\Gamma_\epsilon$  denotes the surface of the half-sphere with radius  $\epsilon$  the first expression on the right side of Eq. (19) becomes:

$$\lim_{\epsilon \rightarrow 0} \int_{\Gamma'} G(\mathbf{r}, \mathbf{r}') \frac{\partial\Phi(\mathbf{r}')}{\partial n} d\Gamma = \lim_{\epsilon \rightarrow 0} \int_{\Gamma' - \Gamma_\epsilon} G(\mathbf{r}, \mathbf{r}') \frac{\partial\Phi(\mathbf{r}')}{\partial n} d\Gamma + \lim_{\epsilon \rightarrow 0} \int_{\Gamma_\epsilon} G(\mathbf{r}, \mathbf{r}') \frac{\partial\Phi(\mathbf{r}')}{\partial n} d\Gamma. \quad (22)$$

With  $d\Gamma_\epsilon = \epsilon^2 \cos \vartheta d\theta d\varphi$  and  $|\mathbf{r} - \mathbf{r}'| = \epsilon$  the second expression on the right side of Eq. (22) vanishes:

$$\lim_{\epsilon \rightarrow 0} \int_{\Gamma_\epsilon} G(\mathbf{r}, \mathbf{r}') \frac{\partial\Phi(\mathbf{r}')}{\partial n} d\Gamma = -\lim_{\epsilon \rightarrow 0} \int_{\Gamma_\epsilon} \frac{1}{4\pi\epsilon} \frac{\partial\Phi(\mathbf{r}')}{\partial n} \epsilon^2 \cos \vartheta d\theta d\varphi = 0. \quad (23)$$

In the same manner, the second contribution to the integral expression on the RHS of Eq. (19) is computed as:

$$\begin{aligned} \lim_{\epsilon \rightarrow 0} \int_{\Gamma'} \frac{\partial G(\mathbf{r}, \mathbf{r}')}{\partial n} \Phi(\mathbf{r}') d\Gamma(\mathbf{r}') &= \lim_{\epsilon \rightarrow 0} \int_{\Gamma' - \Gamma_\epsilon} \frac{\partial G(\mathbf{r}, \mathbf{r}')}{\partial n} \Phi(\mathbf{r}') d\Gamma(\mathbf{r}') \\ &+ \lim_{\epsilon \rightarrow 0} \int_{\Gamma_\epsilon} \frac{\partial G(\mathbf{r}, \mathbf{r}')}{\partial n} \Phi(\mathbf{r}') d\Gamma(\mathbf{r}'). \end{aligned} \quad (24)$$

Unlike in the former case, in Eq. (24), the contribution of the integration over

the  $\epsilon$ -sphere does not vanish since

$$\begin{aligned}
\lim_{\epsilon \rightarrow 0} \int_{\Gamma_\epsilon} \frac{\partial G(\mathbf{r}, \mathbf{r}')}{\partial n} \Phi(\mathbf{r}') d\Gamma(\mathbf{r}') &= - \lim_{\epsilon \rightarrow 0} \int_{\Gamma_\epsilon} \frac{\mathbf{n} \cdot (\mathbf{r} - \mathbf{r}')}{4\pi |\mathbf{r} - \mathbf{r}'|^3} \Phi(\mathbf{r}') d\Gamma(\mathbf{r}') \\
&= \lim_{\epsilon \rightarrow 0} \int_{\Gamma_\epsilon} \frac{1}{4\pi \epsilon^2} \Phi(\mathbf{r}') \epsilon^2 \cos \vartheta d\vartheta d\varphi \\
&= \int_{\vartheta=-\pi/4}^{\vartheta=+\pi/4} \int_{\varphi=0}^{\varphi=\pi} \frac{1}{4\pi} \Phi(\mathbf{r}') \cos \vartheta d\vartheta d\varphi = \frac{1}{2} \Phi(\mathbf{r}). \tag{25}
\end{aligned}$$

Using Eqs. (22-25) the integral equation (19) is re-written for  $\mathbf{r} \in \Gamma$  as

$$\frac{1}{2} \Phi(\mathbf{r}) = \int_{\Gamma} G(\mathbf{r}, \mathbf{r}') \underbrace{\frac{\partial \Phi(\mathbf{r}')}{\partial n}}_{-B^n(\mathbf{r}')} - \Phi(\mathbf{r}') \frac{\partial G(\mathbf{r}, \mathbf{r}')}{\partial n} d\Gamma(\mathbf{r}'). \tag{26}$$

which is called boundary integral equation. From Eq. (26) the tangential components of the magnetic field on the boundary  $B^t = \mathbf{e}_\tau \cdot \mathbf{B} = -\mathbf{e}_\tau \cdot \nabla \Phi(\mathbf{r})$  are computed by:

$$B^\tau = 2 \int_{\Gamma} \mathbf{e}_\tau \cdot \left( \Phi(\mathbf{r}') \nabla_r \frac{\partial G(\mathbf{r}, \mathbf{r}')}{\partial n} + B^n(\mathbf{r}') \nabla_r G(\mathbf{r}, \mathbf{r}') \right) d\Gamma(\mathbf{r}') \tag{27}$$

where  $\mathbf{e}_\tau$  represents the tangential unit vector on the surface element  $d\Gamma(\mathbf{r}')$ . Eq. (26) and (27) have been derived for a bounded region. An infinite volume is treated by introduction of a fictitious surface  $\bar{\Gamma}$  describing a sphere with radius  $\bar{R}$  in the limit  $\bar{R} \rightarrow \infty$ . Consider exemplary Eq. (26) which is re-written including terms from infinity:

$$\begin{aligned}
\frac{1}{2} \Phi(\mathbf{r}) &= \int_{\Gamma} G(\mathbf{r}, \mathbf{r}') \frac{\partial \Phi(\mathbf{r}')}{\partial n} d\Gamma(\mathbf{r}') + \int_{\bar{\Gamma}} G(\mathbf{r}, \mathbf{r}') \frac{\partial \Phi(\mathbf{r}')}{\partial n} d\Gamma(\mathbf{r}') \\
&\quad - \int_{\Gamma} \Phi(\mathbf{r}') \frac{\partial G(\mathbf{r}, \mathbf{r}')}{\partial n} d\Gamma(\mathbf{r}') - \int_{\bar{\Gamma}} \Phi(\mathbf{r}') \frac{\partial G(\mathbf{r}, \mathbf{r}')}{\partial n} d\Gamma(\mathbf{r}'). \tag{28}
\end{aligned}$$

In three dimensions the following asymptotic behavior of the surface element  $d\Gamma$  and the fundamental solution  $G(\mathbf{r}, \mathbf{r}')$  occurs for  $\bar{R} \rightarrow \infty$ :

$$d\Gamma(\mathbf{r}') = |\mathcal{J}| d\varphi d\vartheta, \quad |\mathcal{J}| \sim O(\bar{R}^2), \tag{29a}$$

$$G(\mathbf{r}, \mathbf{r}') \sim O(\bar{R}^{-1}), \quad \mathbf{r} \in \bar{\Gamma}, \tag{29b}$$

$$\frac{\partial G(\mathbf{r}, \mathbf{r}')}{\partial n} \sim O(\bar{R}^{-2}). \tag{29c}$$

where  $\mathcal{J}$  denotes the Jacobian. Combining the regularity condition  $\Phi \propto O(\bar{R}^{-2})$  from (17) at infinity with the asymptotic behavior given in (29a-29c) it is ensured that the integral expressions in (28) that involve  $\bar{R}$  vanish for  $\bar{R} \rightarrow \infty$ .

A discretization of the system (26) and (27) yields an algebraic system of equations which allows the computation of the (unknown) tangential components of the magnetic field. The natural way to define the boundary elements is an application of the tessellation provided by the finite volume discretization on the

domain surface, where every element has one face centered node at which the normal field component  $B^n$  is located (see Fig. 3).

After the subdivision of the surface  $\Gamma$  in "small" boundary elements  $\Gamma_j$  with  $\Gamma = \cup \Gamma_j$  the potential  $\Phi_i = \Phi(\mathbf{r}_i)$  and the tangential field  $B_i^t = B^t(\mathbf{r}_i) = -\mathbf{e}_\tau \cdot (\nabla \Phi_i)$  are given by

$$\begin{aligned} \frac{1}{2}\Phi_i &= -\sum_j \underbrace{\left( \int_{\Gamma_j} \frac{\partial G}{\partial n}(\mathbf{r}_i, \mathbf{r}') d\Gamma'_j \right)}_{\mathcal{H}_{ij}^1} \Phi_j - \sum_j \underbrace{\left( \int_{\Gamma_j} G(\mathbf{r}_i, \mathbf{r}') d\Gamma'_j \right)}_{\mathcal{H}_{ij}^2} B_j^n \\ B_i^t &= \sum_j \underbrace{\left( \int_{\Gamma_j} 2\hat{\mathbf{e}}_\tau \cdot \nabla_r \frac{\partial G}{\partial n}(\mathbf{r}_i, \mathbf{r}') d\Gamma'_j \right)}_{\mathcal{H}_{ij}^3} \Phi_j + \sum_j \underbrace{\left( \int_{\Gamma_j} 2\hat{\mathbf{e}}_\tau \cdot \nabla_r G(\mathbf{r}_i, \mathbf{r}') d\Gamma'_j \right)}_{\mathcal{H}_{ij}^4} B_j^n. \end{aligned} \quad (30)$$

Eq. (30) introduces a global ordering of the quantities  $\Phi$  and  $B^{t,n}$  defined by an explicit mapping of the grid-cell indices  $(ix, iy, iz)$  on a global index  $(i)$  with  $i = 0, 1, 2, \dots, N$  where  $N = 2 \cdot (nz \cdot ny + nz \cdot nx + ny \cdot nx)$  represents the total number of boundary elements. Then  $\Phi, B^{t,n}$  can be considered as large vectors and abbreviating the integral expressions in (30) with  $\mathcal{H}^k (k = 1, \dots, 4)$  the system can be re-written in a matrix representation:

$$\frac{1}{2}\Phi_i = -\mathcal{H}_{ij}^1 \Phi_j - \mathcal{H}_{ij}^2 B_j^n, \quad (31)$$

$$B_i^t = \mathcal{H}_{ij}^3 \Phi_j + \mathcal{H}_{ij}^4 B_j^n. \quad (32)$$

Finally, a linear, non-local expression for the tangential field components in terms of the normal components results:

$$\mathbf{B}^t = \left( \mathcal{H}^3 \otimes \left( \frac{1}{2} \cdot \mathbb{1} - \mathcal{H}^1 \right)^{-1} \otimes \mathcal{H}^2 + \mathcal{H}^4 \right) \otimes \mathbf{B}^n = \mathcal{M} \otimes \mathbf{B}^n. \quad (33)$$

The numerical computation of the matrix elements  $\mathcal{H}_{ij}^k$  is performed applying a standard 2D-Gauss-Legendre Quadrature method. However, for  $i = j$  the integral expressions in Eq. (30) become singular so that  $\mathcal{H}_{ii}^k$  have to be treated separately. Since  $B^t$  is computed from the derivative of  $\Phi$  the scalar potential is only determined except an additional constant. Fixing this constant results in a relation between diagonal and off-diagonal elements of the matrices  $\mathcal{H}^1$  and  $\mathcal{H}^3$  (details see [15]):

$$\mathcal{H}_{ii}^1 = -\frac{1}{2} - \sum_{j \neq i} \mathcal{H}_{ij}^1 \quad \text{and} \quad \mathcal{H}_{ii}^3 = -\sum_{j \neq i} \mathcal{H}_{ij}^3. \quad (34)$$

The matrix elements  $\mathcal{H}_{ii}^2$  are weakly singular and are computed numerically without further difficulties after applying a special cubic coordinate transformation where the Jacobian of the transformation has a minimum at the singularity [20].

The integral expression that determines the diagonal element of  $\mathcal{H}^4$  exhibits a strong singularity with a vanishing Cauchy principal value so that  $\mathcal{H}_{ii}^4$  can be computed by excluding some small  $\epsilon$ -vicinity around  $\mathbf{r}_i$ .



Since the elements of  $\mathcal{H}^k$  only depend on the geometry and the discretization of the problem the computation of  $\mathcal{M}$  has to be carried out only once. However, since the computation of  $\mathbf{B}^t = \mathcal{M} \otimes \mathbf{B}^n$  requires a matrix multiplication with a matrix  $\mathcal{M}$  of size  $(2N \times N)$  a large amount of memory is required for  $\mathcal{M}$  which limits the maximal achievable resolution. This restriction is slightly less severe in cylindrical coordinates where the periodicity in azimuthal direction reduces the necessary size of the matrix  $\mathcal{M}$ .

### 3. Results.

**3.1. Simple test case.** The free decay of a magnetic field is a simple test problem where only the diffusive part of the induction equation ( $\partial_t \mathbf{B} \propto \Delta \mathbf{B}$ ) is considered. A (small) challenge for the scheme arises by initially randomly distributed field components which involves the presence of all (resolvable) modes. The higher modes decay rather fast and the final solution is dominated by the axisymmetric dipole mode which corresponds to the eigenfunction of the system with the lowest eigenvalue. Fig. 4 shows the structure of the decaying field in a cylinder of height  $H = 2$  and radius  $R = 1$  after approximately one diffusion time ( $\tau_{\text{diff}} = \mu_0 \sigma R^2$ ) which is dominated by an axial dipole.

The temporal behavior of the total magnetic energy  $E_{\text{mag}} = (2\mu_0)^{-1} \int \mathbf{B}^2 dV$  is shown in Fig. 5. After the system settles down to its eigensolution (at  $t \sim 0.1\tau_{\text{diff}}$ ) a simple exponential decay  $\propto e^{-\lambda t/\tau_{\text{diff}}}$  is observed.

The influence of the boundary conditions is obvious in comparison with the decay rate in case of *vanishing tangential field* boundary conditions (VTF, dashed curve) where a significant slower decay takes place. Table 1 shows the decay rate for both types of boundary conditions in comparison with the results obtained by [6] applying the integral equation approach (IEA) and a differential equation approach (DEA) where the Laplace equation is solved in the exterior.

The decay rate of the  $m = 0$  mode in case of insulating boundaries is larger than for VTF conditions because of smaller or even vanishing field gradients in the latter case. The decay rate for the  $m = 1$  mode achieved from the FV-BEM scheme is approximately 4% larger than the decay rate obtained from the IEA. The observed deviation between the different schemes might arise through a couple of reasons which will be discussed in the following subsection.

**3.2. Von-Kármán flow.** The experimental realization of a von-Kármán-like flow in the VKS experiment is driven by two counter-rotating propellers located close to the end-plates of the cylindrical vessel. An analytic prescribed velocity field that roughly resembles the mean flow in the VKS experiment is given by the so called MND-flow (Marié-Normand-Daviaud, [21]):

$$\begin{aligned} v_r &= -0.5\pi \cos(\pi z) r(1-r)^2(1+2r) \\ v_\varphi &= 4\epsilon r(1-r) \sin(0.5\pi z) \\ v_z &= (1-r)(1+r-5r^2) \sin(\pi z) \end{aligned} \tag{35}$$

where  $\epsilon$  describes the relation between toroidal and poloidal component of the velocity (here given by  $\epsilon = 0.7259$  which has turned out to be an optimum value for generating a dynamo [21]).

The structure of this flow is essentially dominated by two toroidal and two poloidal cells which are visualized in Fig. 6 where the grey scaled contours represent the azimuthal flow component and the arrows represent the poloidal flow

components. If the Reynolds number – defined as  $Rm = \sigma\mu_0RV_{\max}$  – exceeds a critical value, dynamo action takes place. Detailed examinations of the induction effects of the MND-flow – in particular on the effects of side and lid layers containing a stagnant fluid component that surrounds the active region – can be found in [6]. Here, only simulations without outer fluid layers are discussed.

The initial condition is again given by a divergence-free random field, which – if the applied magnetic Reynolds number exceeds the critical value – after a timespan of about a diffusion time passes into a growing smooth field (Fig. 7) field. The obtained field structure essentially represents the well known banana-cell like behavior ([6, 22]) corresponding to a field dominated by the  $m = 1$  mode (see left hand side of Fig. 7). The right hand side of Fig. 7 presents a snapshot of the streamlines of the magnetic field from a typical simulation ( $Rm = 80$ ) from which the clear dominance of the equatorial oriented dipole solution is apparent. A quantitative comparison between the FV-BEM and the IEA schemes has been done by means of the growth-, respectively decay rates for the  $m = 1$  mode.

If  $Rm \lesssim Rm^{\text{crit}}$  the field decays and the slowest decaying eigenmode can be observed. For the 3D grid based FV-BEM scheme the growth rates have been computed from the temporal behavior of the volume averaged Fourier amplitudes (azimuthal decomposition) of the axial field component<sup>1</sup>. The growth rates of the dynamo (or decaying) state in dependence of the applied  $Rm$  are presented in Fig. 8.

Both schemes provide rather similar results for small and moderate Reynolds numbers. Small but systematic deviations between the IEA and the FV-BEM occur for  $Rm \gtrsim 45$ . The main and most probable reason for this characteristic behavior might be the rather low resolution attainable by the IEA which is restricted to  $20 \times 20$  points in a 2D simulation due to the enormous computational power required by this method. A further influence might be obtained from the coupling of different field modes that necessarily occurs in the 3D FV-BEM scheme whereas the IEA only considers one single mode. However, it seems unlikely that this influence has a remarkable effect since the amplitudes of the non-dominating modes are always suppressed by several orders of magnitude.

For the FV-BEM scheme the critical Reynolds number is obtained from interpolation of the growth rates around the occurrence of dynamo action and is given by  $Rm^{\text{crit}} = 62.6$ . This value is situated slightly above the value reported in [22] ( $Rm^{\text{crit}} = 58$ ) or the results of simulations with the DEA ( $Rm^{\text{crit}} = 61.5$ ) respectively the IEA ( $Rm^{\text{crit}} = 59.6$ ) reported in [6]. For idealizing VTF conditions the critical Reynolds number is computed as  $Rm^{\text{crit}} = 41.2$  (see dotted curve in Fig. 8). The significant deviation between the critical Reynolds number for physical boundaries and for idealizing (VTF) boundaries depends on the geometry of the system and becomes smaller for a larger relation between height and radius. Beside  $Rm^{\text{crit}}$ , a second distinguished point exists, at which the transition of a  $m = 0$  dominated solution to a  $m = 1$  dominated solution proceeds, which occurs at  $Rm \approx 25$ . Below this value the axial dipole dominates the field structure, however, the  $m = 0$  mode never becomes unstable to dynamo action. Note, that for small Reynolds numbers both schemes yield a slight minimum for the decay rate of the  $m = 1$  mode, so that for  $Rm \lesssim 15$  this mode decays faster than without any flow.

**4. Conclusion.** A fast and easy to handle code base for 3D simulations of the kinematic induction equation has been developed which is able to treat in-

---

<sup>1</sup>All components of the magnetic field behave similar, however,  $B_z$  is the dominant component.

insulating boundary conditions in a stringent way. The reliability of the approach has been tested against known results of dynamo action generated by the (analytic prescribed) MND-flow and a good agreement was achieved in comparison with the results of the integral equation approach. The IEA is also able to treat insulating boundary conditions but requires much more computational power and provides less flexibility concerning the addition of further physical effects or geometric constraints.

Significant differences for the critical Reynolds number and the growth rates exist between simplifying boundary conditions and insulating boundaries. These discrepancies become smaller for higher aspect ratios. However, in case of a realistic relation between height and radius as it usually is realized in the laboratory, a thorough consideration of the appropriate boundary conditions is indispensable.

The flexibility of the scheme facilitates the addition of further physical terms like an  $\alpha$ -effect as additional dynamo source or the consideration of temporal fluctuations of the mean flow. A direct extension of the scheme which will be presented in a subsequent paper will be able to consider conductivity/permeability inhomogeneities.

**Acknowledgements.** Financial support from Deutsche Forschungsgemeinschaft (DFG) in frame of the Collaborative Research Center (SFB) 609 is gratefully acknowledged.

#### REFERENCES

1. J. LARMOR. How could a rotating body such as the sun become a magnet? *Rep. Br. Assoc. Adv. Sci. A*, (1919), pp. 159–160.
2. A. GAILITIS, ET AL. Detection of a Flow Induced Magnetic Field Eigenmode in the Riga Dynamo Facility. *Phys. Rev. Lett.*, vol. 84 (2000), pp. 4365–4368.
3. R. STIEGLITZ AND U. MÜLLER. Experimental demonstration of a homogeneous two-scale dynamo. *Phys. Fluids*, vol. 13 (2001), pp. 561–564.
4. R. MONCHAUX, ET AL. Generation of a Magnetic Field by Dynamo Action in a Turbulent Flow of Liquid Sodium. *Phys. Rev. Lett.*, vol. 98 (2007), no. 4, p. 044502.
5. R. AVALOS-ZUÑIGA AND F. PLUNIAN. Influence of inner and outer walls electromagnetic properties on the onset of a stationary dynamo. *Eur. Phys. J. B*, vol. 47 (2005), pp. 127–135.
6. F. STEFANI, ET AL. Ambivalent effects of added layers on steady kinematic dynamos in cylindrical geometry: application to the VKS experiment. *Eur. J. Mech. B*, vol. 25 (2006), pp. 894–908.
7. R. TEYSSIER, S. FROMANG, AND E. DORMY. Kinematic dynamos using constrained transport with high order Godunov schemes and adaptive mesh refinement. *J. Comp. Phys.*, vol. 218 (2006), pp. 44–67.
8. J. L. GUERMOND, J. LÉORAT, AND C. NORE. A new Finite Element Method for magneto-dynamical problems: two-dimensional results. *Eur. J. Mech. B*, vol. 22 (2003), pp. 555–579.
9. A. GAILITIS, ET AL. Riga dynamo experiment and its theoretical background. *Phys. Plasmas*, vol. 11 (2004), pp. 2838–2843.
10. J. L. GUERMOND, R. LAGUERRE, J. LÉORAT, AND C. NORE. A finite element interior penalty method for MHD in heterogenous domains. In P. WESSELING, E. OÑATE, AND J. PÉRIAUX, editors, *European Conference on Computational Fluid Dynamics ECCOMAS CFD 2006* (TU Delft, Netherlands, 2006).
11. A. TILGNER. A kinematic dynamo with a small scale velocity field. *Physics Letters A*, vol. 226 (1997), pp. 75–79.

Mode $m$	DEA	IEA	FV-BEM	FV (VTF)
0	—	—	-7.94	-5.81
1	-8.13	-8.42	-8.75	-7.20

Table 1: Decay rates for the free decay of an initial random field in a cylindrical geometry for the dipole mode ( $m = 0$ ) and the first non-axisymmetric mode ( $m = 1, \propto \cos \varphi$ ) obtained from a differential equation approach (DEA), the integral equation approach (IEA, see [6] for a description of both methods and the results), the hybrid finite volume-boundary element method presented here and the finite volume approach with vanishing tangential field conditions on the boundary.

12. M. XU, F. STEFANI, AND G. GERBETH. The integral equation method for a steady kinematic dynamo problem. *J. Comp. Phys.*, vol. 196 (2004), pp. 102–125.
13. M. XU, F. STEFANI, AND G. GERBETH. Integral equation approach to time-dependent kinematic dynamos in finite domains. *Phys. Rev. E*, vol. 70 (2004), no. 5, p. 056305.
14. C. A. BREBBIA, J. C. F. TELLES, AND L. C. WROBEL. *Boundary Element Techniques* (Springer-Verlag, 1984).
15. A. B. ISKAKOV, S. DESCOMBES, AND E. DORMY. An integro-differential formulation for magnetic induction in bounded domains: boundary element-finite volume method. *J. Comp. Phys.*, vol. 197 (2004), pp. 540–554.
16. E. HABER AND U. M. ASCHER. Fast Finite Volume Simulation of 3d electromagnetic problems with highly discontinuous coefficients. *SIAM J. Sci. Comput.*, vol. 22 (2001), pp. 1943–1961.
17. J. M. STONE AND M. L. NORMAN. ZEUS-2D: A radiation magnetohydrodynamics code for astrophysical flows in two space dimensions. I - The hydrodynamic algorithms and tests. *Astrophys. J.-Suppl. Ser.*, vol. 80 (1992), pp. 753–790.
18. J. M. STONE AND M. L. NORMAN. ZEUS-2D: A Radiation Magnetohydrodynamics Code for Astrophysical Flows in Two Space Dimensions. II. The Magnetohydrodynamic Algorithms and Tests. *Astrophys. J.-Suppl. Ser.*, vol. 80 (1992), p. 791.
19. G. S. CONSTANTINESCU AND S. K. LELE. A Highly Accurate Technique for the Treatment of Flow Equations at the Polar Axis in Cylindrical Coordinates Using Series Expansions. *J. Comp. Phys.*, vol. 183 (2002), pp. 165–186.
20. J. TELLES. A self-adaptive co-ordinate transformation for efficient numerical evaluation of general boundary element integrals. *Int. J. Num. Meth. Eng.*, vol. 24 (1987), no. 5, pp. 959–973.
21. L. MARIÉ, C. NORMAND, AND F. DAVIAUD. Galerkin analysis of kinematic dynamos in the von Kármán geometry. *Phys. Fluids*, vol. 18 (2004), pp. 017102–+.
22. F. RAVELET, A. CHIFFAUDEL, F. DAVIAUD, AND J. LÉORAT. Toward an experimental von Kármán dynamo: Numerical studies for an optimized design. *Phys. Fluids*, vol. 17 (2005), pp. 7104–+.

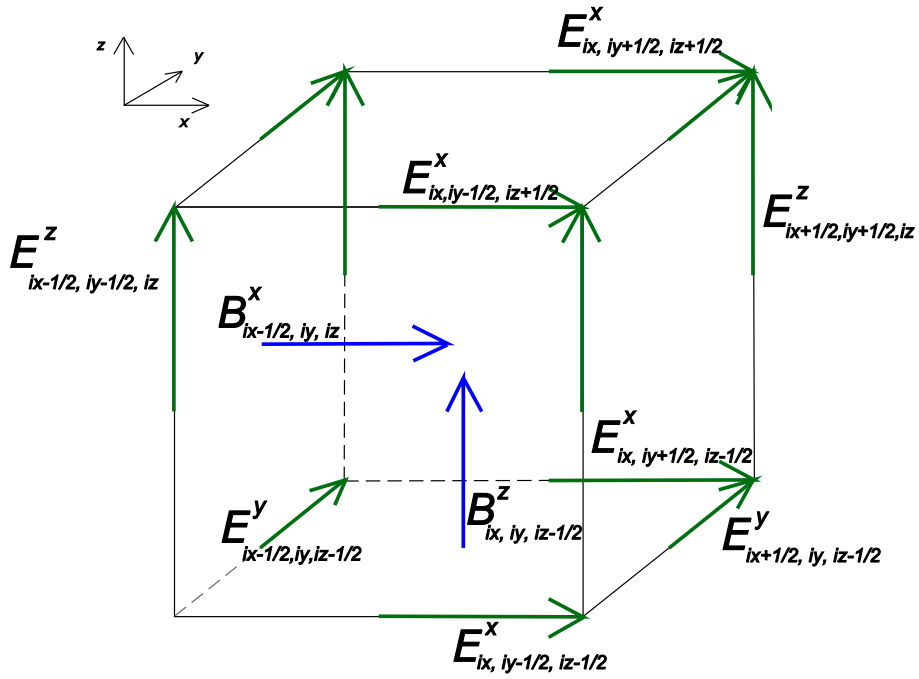


Figure 1: Localization of the components of the electric/magnetic field on the Cartesian staggered mesh. Not all components are labeled for the reason of clarity.

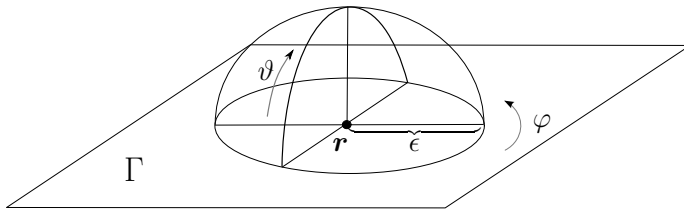


Figure 2: Enlarged domain around the source point  $\mathbf{r}$  located on the boundary surface  $\Gamma$ . The boundary integral equation is evaluated over an extended domain  $\Gamma + \Gamma_\epsilon$  in the limit  $\epsilon \rightarrow 0$ .

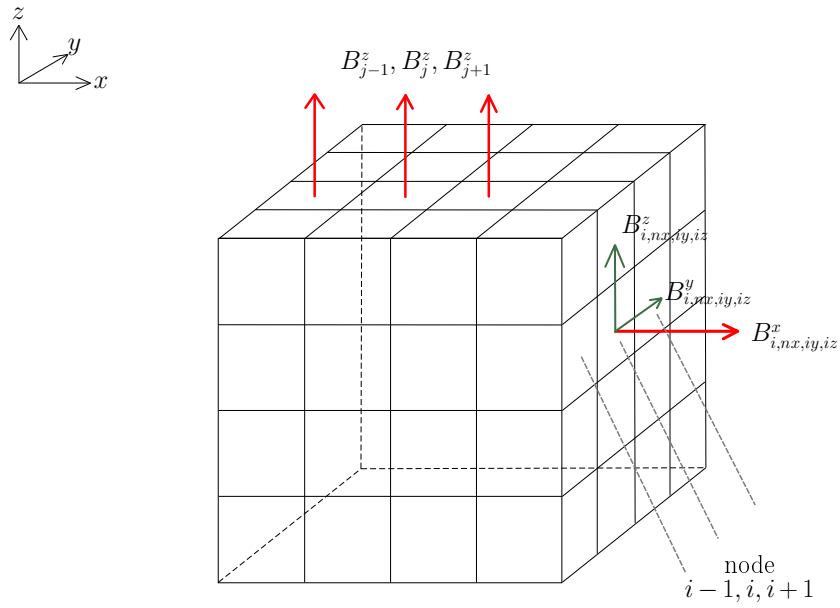


Figure 3: Grid structure and boundary element discretization.  $i, j$  denote a global ordering number.

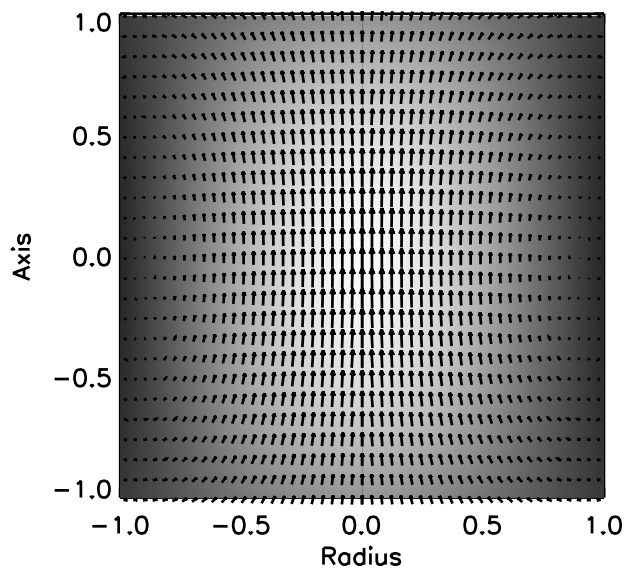


Figure 4: Free decay of an initially random magnetic field. Snapshot of the field structure after one diffusion time. Note the non-vanishing contributions of the tangential components at the boundary caused by the insulating boundary conditions.

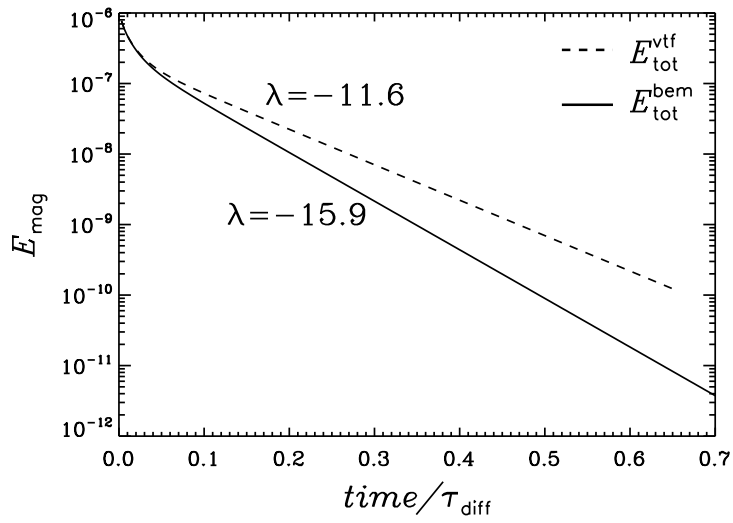


Figure 5: Growth rate of a freely decaying magnetic field in a cylinder. The solid (dashed) curve shows the total energy applying insulating (vanishing tangential field) boundary conditions.

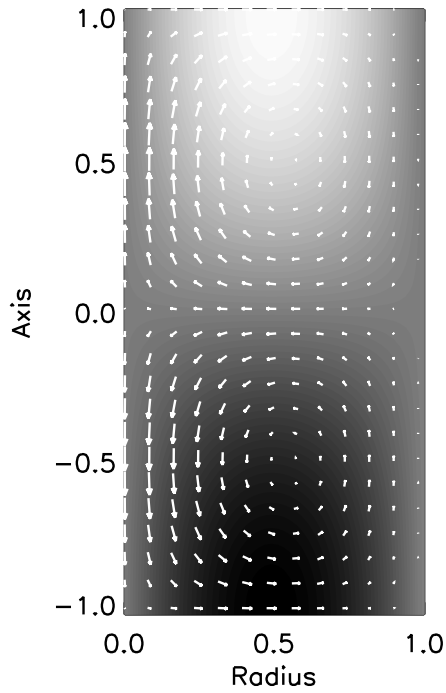


Figure 6: Toroidal (shaded contours) and poloidal (arrows) components of the von-Kármán-like flow prescribed by Eq. (35).



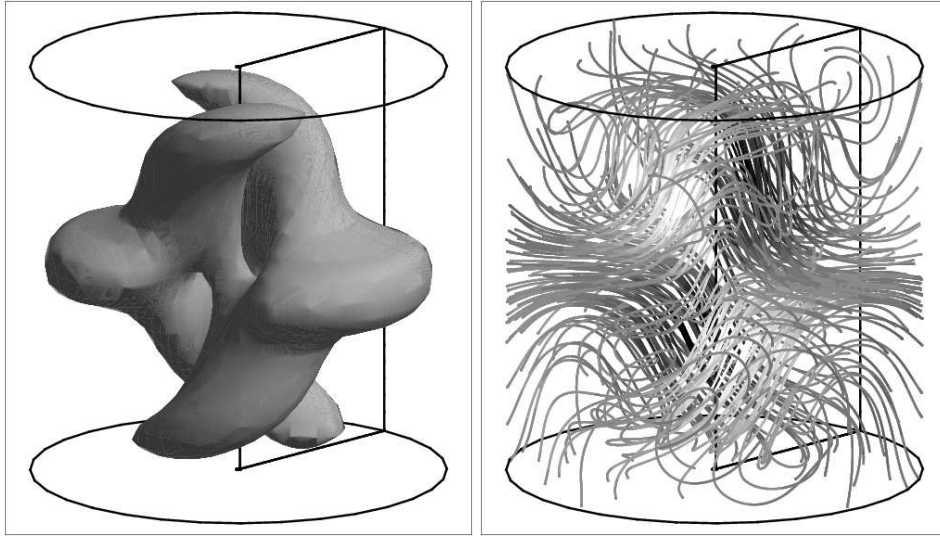


Figure 7: Left panel: Isosurface of the magnetic energy at 20% of the maximum value. Right panel: time snapshot of the magnetic field structure represented by the streamlines.  $Rm = 80$ .

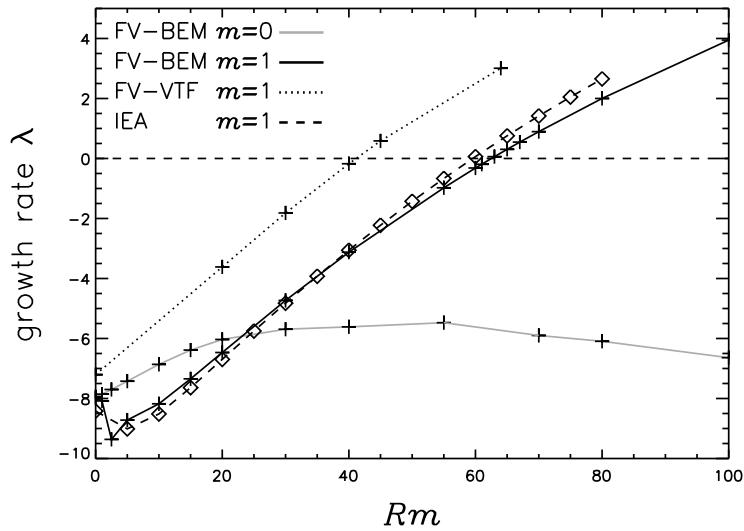


Figure 8: Growth rate of the dominating modes ( $m = 0$ , grey solid curve and  $m = 1$ , black solid curve) in dependence of the magnetic Reynolds number  $Rm$ . The black dashed line corresponds to the growth rates of the  $m = 1$  mode obtained from the IEA [6]. The dotted curve shows the results for vanishing tangential field conditions (VTF).